Physics of the Earth and Planetary Interiors 366 (2025) 107409

Contents lists available at ScienceDirect

Physics of the Earth and Planetary Interiors

journal homepage: www.elsevier.com/locate/pepi

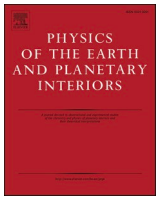

Mechanisms of two P-phase observations in earthquakes within the upper mantle beneath Northeast Taiwan: Insights from 2D waveform simulations

Hung-Yu Yen [a,b], Po-Fei Chen [a,*], Mei Chien [a,1]

[a] Department of Earth Sciences, National Central University, ROC
[b] Taiwan International Graduate Program (TIGP) – Earth System Science Program, (ESS) Academia Sinica and National Central University, ROC

ARTICLE INFO

Keywords:
Formosa array
Two P-phase observations
Eurasian lithosphere boundary
High-velocity mantle wedge

ABSTRACT

Understanding the upper mantle structures beneath northeast Taiwan is crucial for interpreting the region's geodynamics. The deployment of the Formosa Array since 2017 has facilitated this investigation. In this study, we thoroughly examine the observations of two P phases from a representative deep earthquake, starting with a compilation of arrival time patterns and waveform characteristics, followed by two-dimensional waveform simulations. After successfully reproducing the key observations using models that include a high Vp anomaly in the mantle wedge above the Ryukyu subduction zone and a slightly faster Eurasian lithosphere to the west, we conclude that the second P phase originates from a head wave along the sub-vertical boundary of the Eurasian lithosphere. These two-dimensional model structures also replicate the observed arrival time patterns of nearby events with two P phases. The results of this study provide alternative constraint on the boundary between the Philippine Sea Plate and the Eurasian Plate at the surface. The findings support the active role of the Eurasian Plate in accommodating the northwesterly-indented Philippine Sea Plate slab beneath northeast Taiwan, rather than a passively torn model.

1. Introduction

Taiwan is located at the convergent boundary between the Philippine Sea Plate (PSP) and the Eurasian Plate (EUP), where the convergence rate is approximately 8 cm/year in a northwesterly direction (Yu et al., 1997). The Taiwan orogeny, resulting from this convergence, is driven by the collision between the north-south trending Luzon Arc and the northeast-southwest trending Chinese continental shelf, which propagates southwestward across Taiwan (Ho, 1986). Consequently, the southwesterly distance along Taiwan corresponds to the evolution of arc-continent collision over time, characterized by incipient, ongoing, and post-collision stages in southern, central, and northern Taiwan, respectively (Wu et al., 1997). The PSP-EUP convergence is currently accommodated through the east-dipping Manila Trench offshore from southern Taiwan, the ongoing orogeny in central Taiwan, and the north-dipping Ryukyu Trench offshore from northeastern Taiwan. In other words, the PSP-EUP convergence reverses the subduction polarity from the east-dipping Manila Trench to the north-dipping Ryukyu Trench as one moves northward across Taiwan (Su et al., 2019). This reversal reflects the consumption of the South China Sea oceanic lithosphere (Chen et al., 2004), followed by arc-continent collision and post-collision processes (Fig. 1).

In the upper mantle beneath northeast Taiwan, the mechanism by which the space previously occupied by the EUP slab accommodates the northwesterly indented PSP slab remains an open question. Two main hypotheses have been proposed: one posits an active role, suggesting that the EUP slab detaches due to its own negative buoyancy following the arc-continent collision (Teng, 1996; Teng et al., 2000; Bina et al., 2020); the other suggests a passive role, where the EUP is torn by the northwestern indentation of the PSP (Lallemand et al., 2001). Therefore, understanding the upper mantle structures beneath northeast Taiwan is crucial for distinguishing between different geodynamic models of subduction polarity reversal and the region's in situ tectonic evolution (Wu et al., 2009).

Since 2017, a dense seismic array known as the Formosa Array (FA) has been deployed in northern Taiwan (Institute of Earth Sciences, Academia Sinica, Taiwan, 2017)). This array consists of 146 broadband stations with an average spacing of approximately 5 km (Fig. 1). The primary objective of the FA is to enhance seismic imaging of magma reservoirs and other subsurface structures in the region. One of the most

* Corresponding author.
E-mail address: bob@ncu.edu.tw (P.-F. Chen).
[1] Now at Department of Earth, Environmental, and Planetary Sciences, Rice University

https://doi.org/10.1016/j.pepi.2025.107409
Received 21 October 2024; Received in revised form 29 April 2025; Accepted 12 June 2025
Available online 13 June 2025

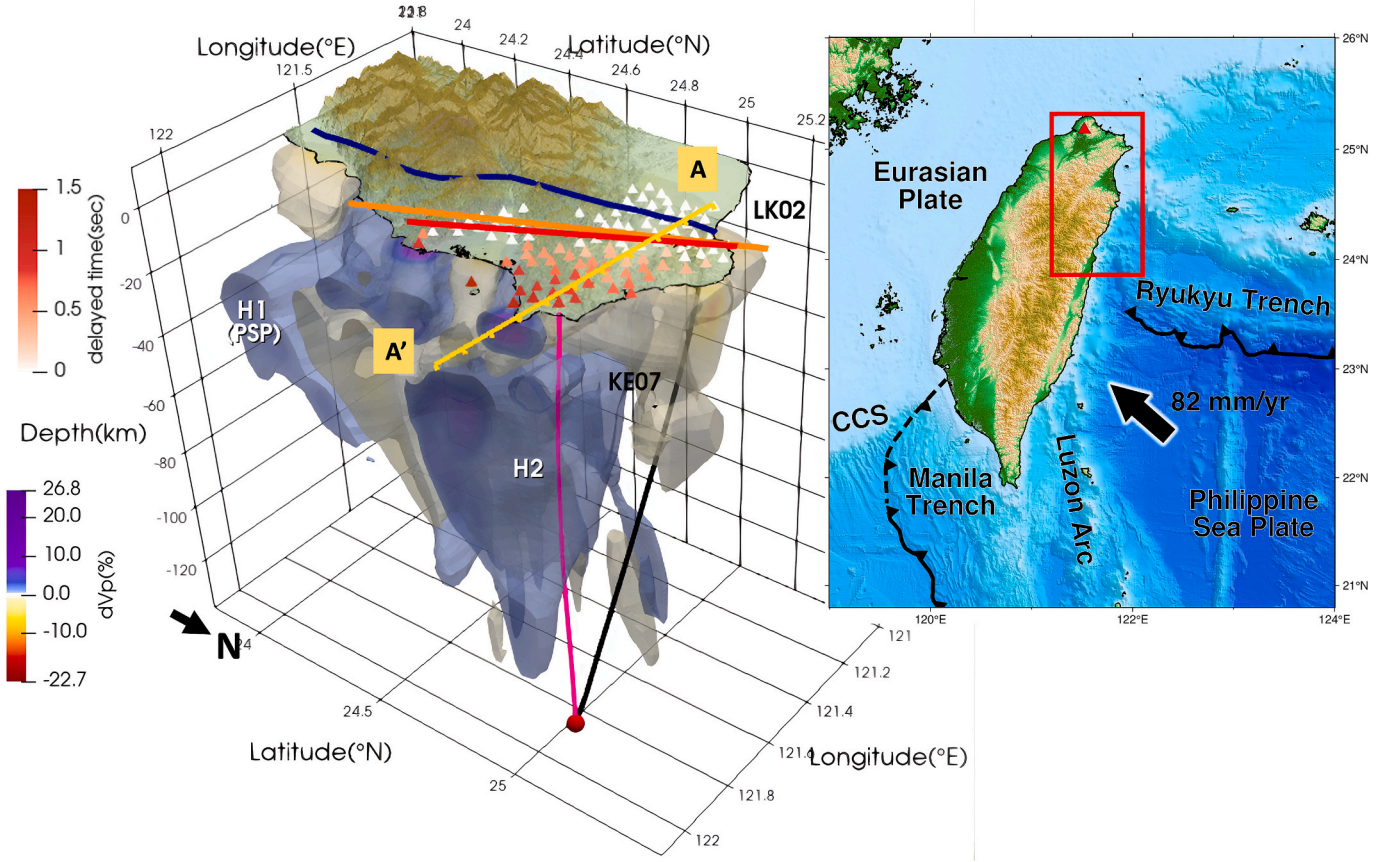

Fig. 1. (Left) High-resolution 3D P-wave velocity anomalies beneath North Taiwan, adopted from Su et al. (2019), with H1 and H2 denoting the high anomalies of the PSP slab and the mantle wedge, respectively. The triangles indicate the distribution of the Formosa Array, with the time delay between P1 and P2 at each station observed from the data of the 0312 event (red circle at 121.86°E, 25.02°N, 138 km), colour-coded. The results of ray tracing indicate that the two P arrivals tend to pass through H2 (pink line to KE07) as opposed to the single P arrivals (black line to LK02). AA' is the profile for 2D waveform simulation. Red line: ELB by stations with zero *P1-P2* delay time. Orange line: surface projection of NW PSP termination from Ko et al. (2012). Blue line: same as the orange line but from Wu et al. (2009). (Right) Tectonic settings of Taiwan, with the region shown in the left figure outlined in a red box and the Tatun volcano indicated by a red triangle. The black arrow denotes the relative motion of the plate. (CCS: Chinese Continental Shelf). (For interpretation of the references to colour in this figure legend, the reader is referred to the web version of this article.)

intriguing observations made with the FA is the detection of a later P phase (P2) in the data from deep earthquakes (~50–150 km) beneath northeastern Taiwan and offshore, with delays of less than 4 s from the first P phase (P1).

The mechanism behind the P2 phase was initially attributed to a reflection boundary at depths of 80–110 km beneath the Tatun volcano group, dipping in the opposite direction to the subducting slab (Lin et al., 2019). This initially proposed simple 2-D dipping plane was later revised to a 3-D scattering obstacle reflecting seismic energy in all directions, resulting in the P2 phase as recorded by all FA stations. For data from four events, four individual mantle wedge diapirs were proposed as the corresponding scattering obstacles. Ray tracing results locate all four sources at depths of 60 to 90 km directly beneath the magma reservoirs (Lin et al., 2021).

However, both studies by Lin et al. (2019) and Lin et al. (2021) are based on the ray-tracing method to fit the arrival times of P1 and P2 without considering waveform information. The only exception is that Lin et al. (2019) used the focal mechanism of the March 12, 2019, event (hereafter referred to as the 0312 event) to explain the larger amplitude of P2 compared to P1. Additionally, it is unlikely that the obstacles scatter energy exclusively from the corresponding event and not the other three events.

In this study, we first focus on the data from the most prominent P2 observations (the 0312 event) and conduct a 2D waveform simulation along the most representative profile. Using velocity structures based on recent tomography studies, which incorporate an artificial distinct subvertical boundary for the fast Eurasian lithosphere, we successfully reproduce the majority of waveform characteristics, thus proposing an alternative model. Secondly, we compile earthquakes that exhibit P2, as recorded by FA stations, and correlate the source distributions with arrival time patterns within the framework of the proposed model to validate a 3D extension.

2. Material and methods

2.1. Observations and determination of 2D profile

The ground displacements of the 0312 event as recorded by FA stations were plotted as a function of epicentral distance (ED) after the instrument was removed. The patterns of directed arrivals exhibit two distinct P phases (labeled as P1 and P2) for ED greater than 25 km and a single phase (labeled as P) for ED less than 25 km, either due to the merging of the two phases or the absence of one phase (Fig. 2a). We visually pick the arrival times of P1 and P2, then determine the P2-P1 delayed times, which were colour-coded with a range from 0 to ~1.45 s for each station. The resulting P2-P1 delayed-time pattern is inversely proportional to ED. Based on this pattern, we extracted the observation along profile AA' (Fig. 1), which is the most representative of the overall waveform effects, as a target for 2D waveform simulations (Fig. 2b).

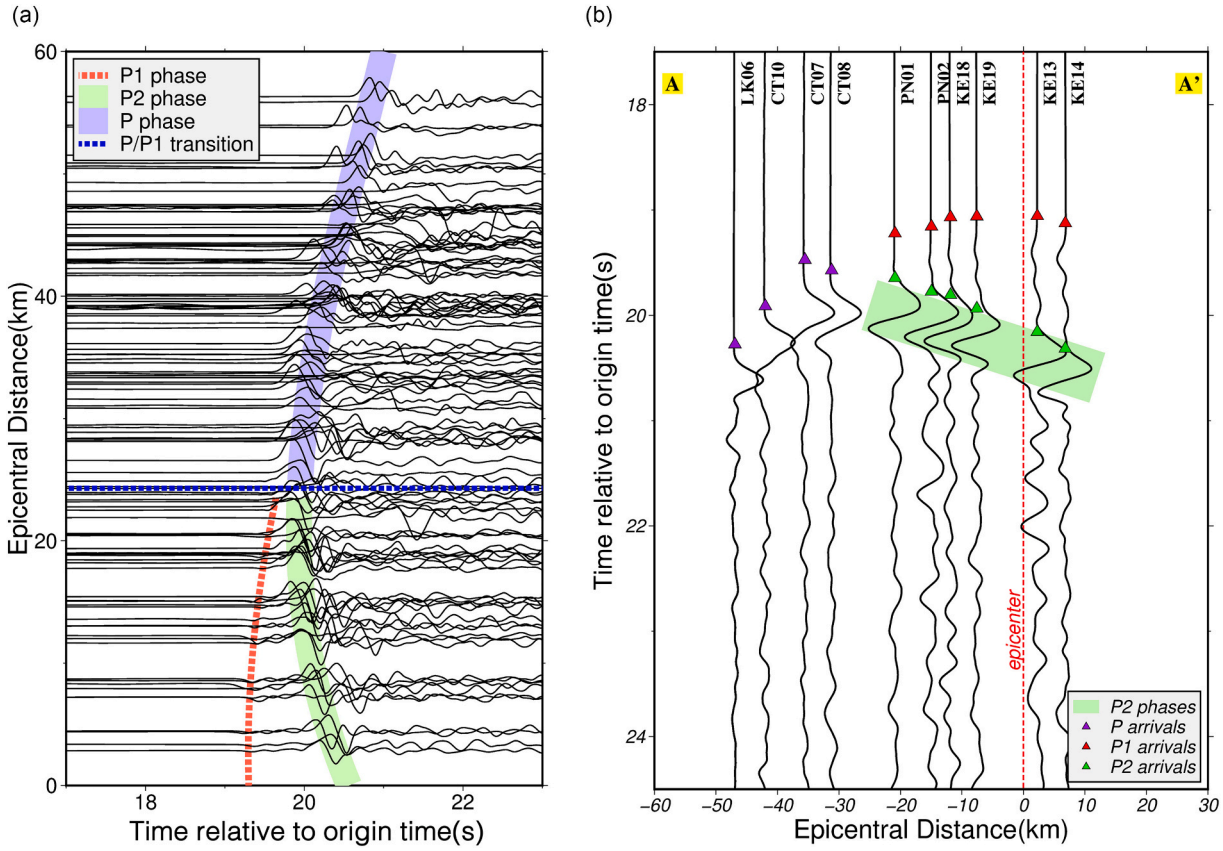

Fig. 2. (a) Vertical displacements of the 0312 event, as recorded by all FA stations, with P1, and P2 labeling the patterns of two first arrival phases for epicentral distance less than 25 km (blue dashed line) and P representing the single phase for distance greater than 25 km. (b) The arrival time patterns and waveform characteristics for FA stations along profile AA'. The location of the epicenter is marked by a red dashed line, and the picked arrival times of P, P1 and P2 are marked by purple, red, and green triangles, respectively. The reverse pattern of *P2* is highlighted in green. (For interpretation of the references to colour in this figure legend, the reader is referred to the web version of this article.)

Before conducting simulations, we compile and summarize the waveform characteristics along the profile as follows (Fig. 2): (C1) Although the arrival times of P1 generally follow the trend of P, indicating shorter travel times with smaller ED, the waveforms of P2 closely resemble those of P in terms of amplitude and phase. (C2) The arrival times of P2 exhibit a reverse pattern, with longer travel times at smaller EDs, leading to an anticorrelation between the delayed time of P2-P1 and ED. (C3) Not only are the amplitudes of P1 much smaller than those of P2 and P, but their phases are also almost opposite to those of P2 and P.

2.2. 2D waveform modeling

To investigate the mechanisms underlying the aforementioned observations, we conducted 2D waveform simulations using visco-elastic finite-difference schemes (Maeda et al., 2017). The purpose of these simulations was to reproduce the compiled waveform characteristics along profile AA' and provide explanations for the observed mechanisms. We began with a 1D velocity model (ak135, Kennett et al., 1995) and referred to the results of 3D tomography across profile AA' (Fig. 3a, Su et al., 2019; Fig. 3b, Huang et al., 2014) for initial adjustments, followed by manual modifications in a trial-and-error approach.

First, we applied an overall 3 % reduction in velocity at depths greater than 20 km to account for the warmer mantle wedge. Secondly, based on Fig. 3a, we inserted an 8 % high-velocity anomaly with a similar but simplified shape at the location of H2. Finally, to replicate the detected boundary between EUP lithosphere (EL) and the PSP (Fig. 3b), we imposed a 3 % velocity increase to the left of profile AA', bounded by the EL boundary (ELB) (Fig. 4a). The 2D waveform simulations were conducted within a scope of 100 × 150 km^2 in horizontal and vertical dimensions, respectively. With a grid spacing of 0.04 km in both dimensions, we were able to simulate waveforms up to ~4 Hz. The Perfectly Matched Layer (PML, Zhang and Shen, 2010) scheme was used as the absorbing boundary condition. The source parameters were based on the moment-tensor solution derived from the waveforms of the Central Weather Administration Seismographic Network.

(https://scweb.cwa.gov.tw/zh-tw/earthquake/cmt/2019031304191553016, CWA, 2012) rise time of 0.6 s (Fig. 4). Fig. 4b shows the optimal velocity models used to reproduce the observations along profile AA' in a trial-and-error approach, with a homogeneous Q_P of 1000 and Q_S of 500. The waveform fitting results are shown in Fig. 5, along with synthetics of virtual stations. Fig. S1 shows the animation of waveform propagation.

3. Results

The arrival time patterns and waveform characteristics of P, P1, and P2 are largely reproduced by the optimal velocity model, which includes a high-velocity anomaly in the mantle wedge (H2) and a subvertical Eurasian lithospheric boundary (ELB) to the west of the source as the main structures. We examine snapshots as a function of time to investigate the mechanisms of each phase, leading to the following conclusions: (I) The P1 phase corresponds to waves propagating upward (slightly to the east) and penetrating H2 to the surface. (II) The P phase corresponds to waves propagating upward to the west and refracting into the Eurasian lithosphere before reaching the surface. (III) The P2 phase corresponds to waves propagating upward, slightly to the west, and incident upon ELB at a critical angle. This scenario is analogous to a

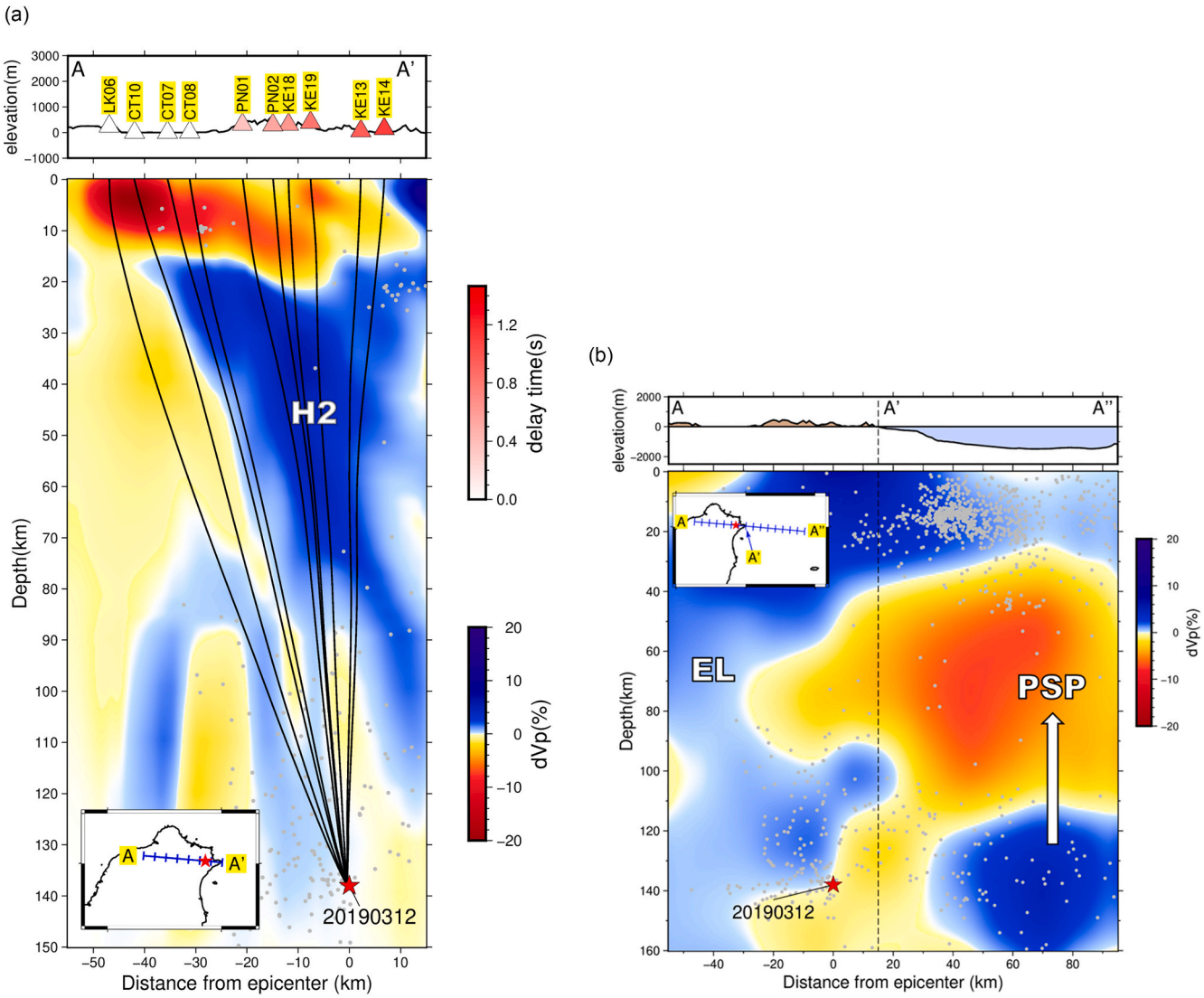

Fig. 3. (a) Velocity anomalies across profile AA' (location shown in inset) adopted from Su et al. (2019), with the hypocenter (red star) and rays (black lines) to stations along profile AA' (top panel, with colour-keyed delayed time from Fig. 1) shown. Gray dots represent background seismicity relocated by Wu et al. (2008) (b) Similar to (a), but with the profile extended eastward to A"(as opposed to A', marked by the black dashed line) and the velocity anomalies adopted from Huang et al. (2014). The corresponding Eurasian lithosphere (EL) and Philippine Sea Plate (PSP) are labeled. The red star marks the hypocenter of the 0312 event. The upper panel displays the topography. (For interpretation of the references to colour in this figure legend, the reader is referred to the web version of this article.)

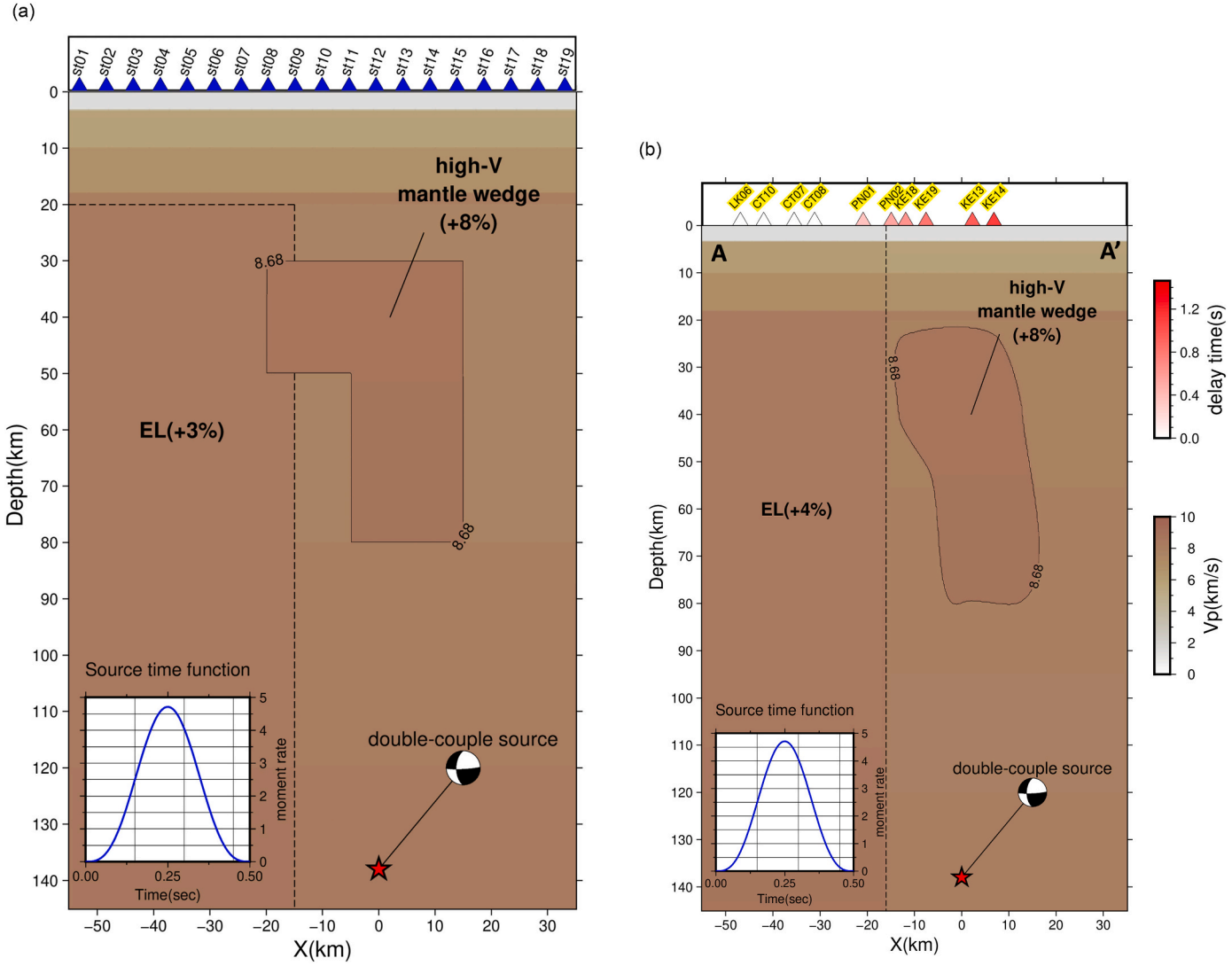

Fig. 4. (a) Initial setup of velocity structures along profile AA' for 2D waveform simulation. Note the artificially imposed EL boundary (vertical dashed line at −15 km). The horizontal distance is measured relative to the epicenter of the 0312 event, with the double-couple solution and adopted source time function indicated. The locations of the virtual array are shown at the top. (b) The optimal velocity models for fitting the waveform characteristics of FA stations along profile AA'. The stations used and their corresponding delay times are shown at the top.

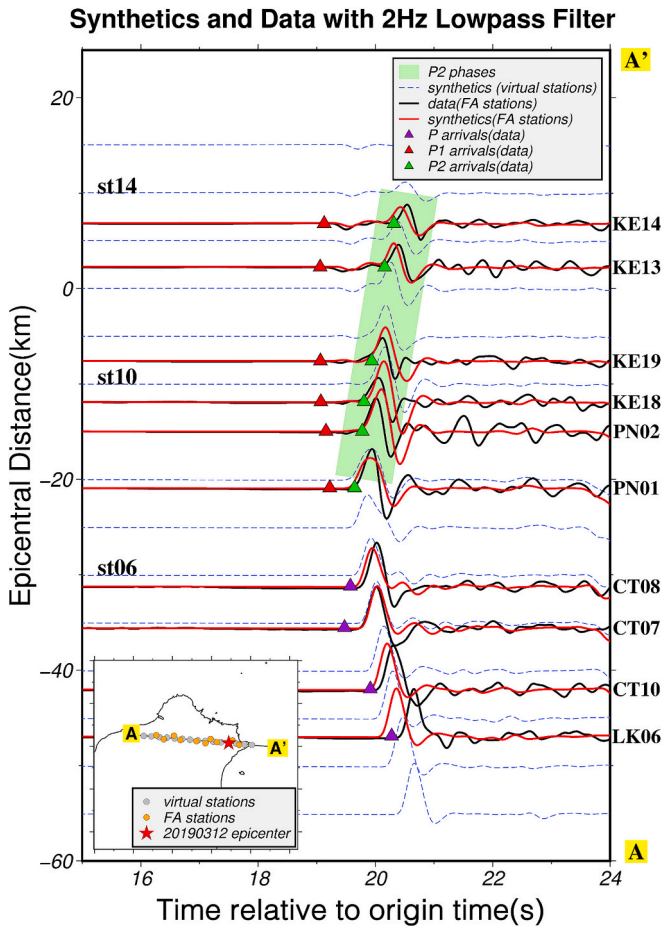

Fig. 5. The observations (solid black lines) and synthetic waveforms (solid red lines) for FA stations profile AA'. The blue dashed lines represent the synthetics of virtual stations along profile AA', spaced at 5 km intervals. The distribution of these stations is illustrated in the inset. The picked arrival times of P, P1 and P2 are marked by purple, red, and green triangles, respectively. The reverse pattern of *P2* is highlighted in green. (For interpretation of the references to colour in this figure legend, the reader is referred to the web version of this article.)

head wave, which radiates energy with the same critical angle back to the east of the surface while propagating along the ELB (Fig. 6).

The mechanisms concluded for the P, P1, and P2 phases can explain the waveform characteristics as follows. For (C1), since both P and P1 are direct arrivals, the combined patterns of arrival times generally increase with ED. Both P and P2 originate from seismic energy with westerly upward radiation, sharing similar source effects and waveform phases, with those of P2 being slightly modulated by critical-angle incidence. For (C2), the observation is misleading due to the lack of observations eastward of the source. The moveout of P2 corresponds to the upward extension of ELB to the surface (Fig. 4b), which is around 30 km west of the epicenter. Farther west of the epicenter is indeed closer to the ELB, thus exhibiting shorter arrival times. The arrival time of P2 is proportional to the distance from the ELB, as demonstrated by synthetic waveforms from virtual stations east of the epicenter (Fig. 5). For (C3), because the nodal point of the source focal mechanism is nearly vertically upward, the slightly easterly upward radiation of P1 is close to the nodal point, resulting in small amplitude and an opposite phase relative to the westerly upward-propagating P and P2.

4. Discussion

In this study, we aim to reproduce the observations of two P phases not only through arrival-time patterns but also by analyzing waveform characteristics. Although the results of 3D tomographic studies were used to build the initial velocity model for the 2D profile across AA', the tomographic models alone could not explain the observations, as suggested by our unsuccessful simulations. This aligns with the conclusion that P2 corresponds to the head wave propagating along an imposed boundary (ELB). Since travel-time data are insensitive to sharp boundaries of velocity contrast (e.g., ELB), tomographic studies tend to smooth out these sharp velocity contrasts. This study demonstrates the importance of incorporating waveform characteristics in structural studies.

The resulting 2D model was established based on the profile (AA') that best represents the overall waveform effects. This 2D approximation seems essential for addressing the complex arrival-time patterns and waveform characteristics. In this study, we examine the spatial applicability of the 2D model by first compiling earthquakes with similar observations of two P phases, and secondly, simulating the waveforms of those earthquakes at FA stations along the AA' profile, then comparing them with the observations. Note that this approach projects the source onto the AA' profile, which may introduce some error.

We selected earthquakes with magnitudes ranging from 3.5 to 6, occurring between 2018 and 2022 within the coordinates 121.5°E to 123.5°E and 24.5°N to 25.5°N, at depths greater than 80 km. The earthquake data from FA stations were examined based on the following criteria for further simulations: (1) the waveforms exhibit two distinct P arrivals, with P1 being weaker than P2; (2) the time delay between the two P phases is less than 2 s; (3) both P phases are observed at stations across the AA' profile. As a result, we identified four additional events that met the criteria (Fig. 7). An interesting pattern was observed in Fig. 7, where events exhibiting two P phases tended to be deeper (depth $>$ 100 km) and in proximity to the AA'.

We aim to demonstrate that the AA' 2D velocity model can reproduce the two-P observations of the four events to some extent. The proximity of the events to the AA' profile validates the simulation using the 2D velocity model across the AA' profile. The AutoBATS moment tensor solution was adopted for each event (https://tecdc.earth.sinica.edu.tw/FM/AutoBATS/; Jian et al., 2018). Regarding observations, the use of linear array stations does not necessarily follow the AA' profile but was selected based on nearby azimuths to maximize the number of available stations for displaying travel time patterns and waveform characteristics. For the simulations, we projected the earthquake epicenter onto the AA' profile as the source location and simulated its propagation along AA' as recorded by a virtual array along the profile (Fig. 8).

After examining the observed and synthetic data for the four events shown in Fig. 8, we conclude that the synthetics based on the AA' 2D velocity model generally succeed in reproducing the observed arrival time patterns, although they are less successful in capturing the waveform characteristics, likely due to the simplifications made in the simulation. This conclusion also suggests that the 2D velocity model derived from the AA' profile is spatially extendable, possibly to the region of the four events. While three out of the four events are located east of ELB, showing mechanisms and observations similar to the 0312 event, the 20,220,507 event occurs to the west of ELB and warrants further investigation. For this event, the two P phases are observed west of the AA' profile, with delayed times increasing toward the west (Fig. 8d). Upon reviewing the synthetic snapshots (Fig. 9), we conclude that the westward-propagating P2 phase originates from a head wave along the west side of H2, a high-velocity anomaly in the mantle wedge.

In the 2D simulation of this study, we do not consider (a) the boundary of the Philippine Sea slab, (b) crustal anomalies, or (c) attenuation anomalies in the mantle wedge for the following reasons. For (a), deep earthquakes are most likely intermediate-depth events located on the top layer of the Philippine Sea slab. For upward-propagating waves, the influence from the high-velocity slab below the source is minimal and remains consistent from the top slab boundary proxy to the source. For (b), lateral variations in the waveform along

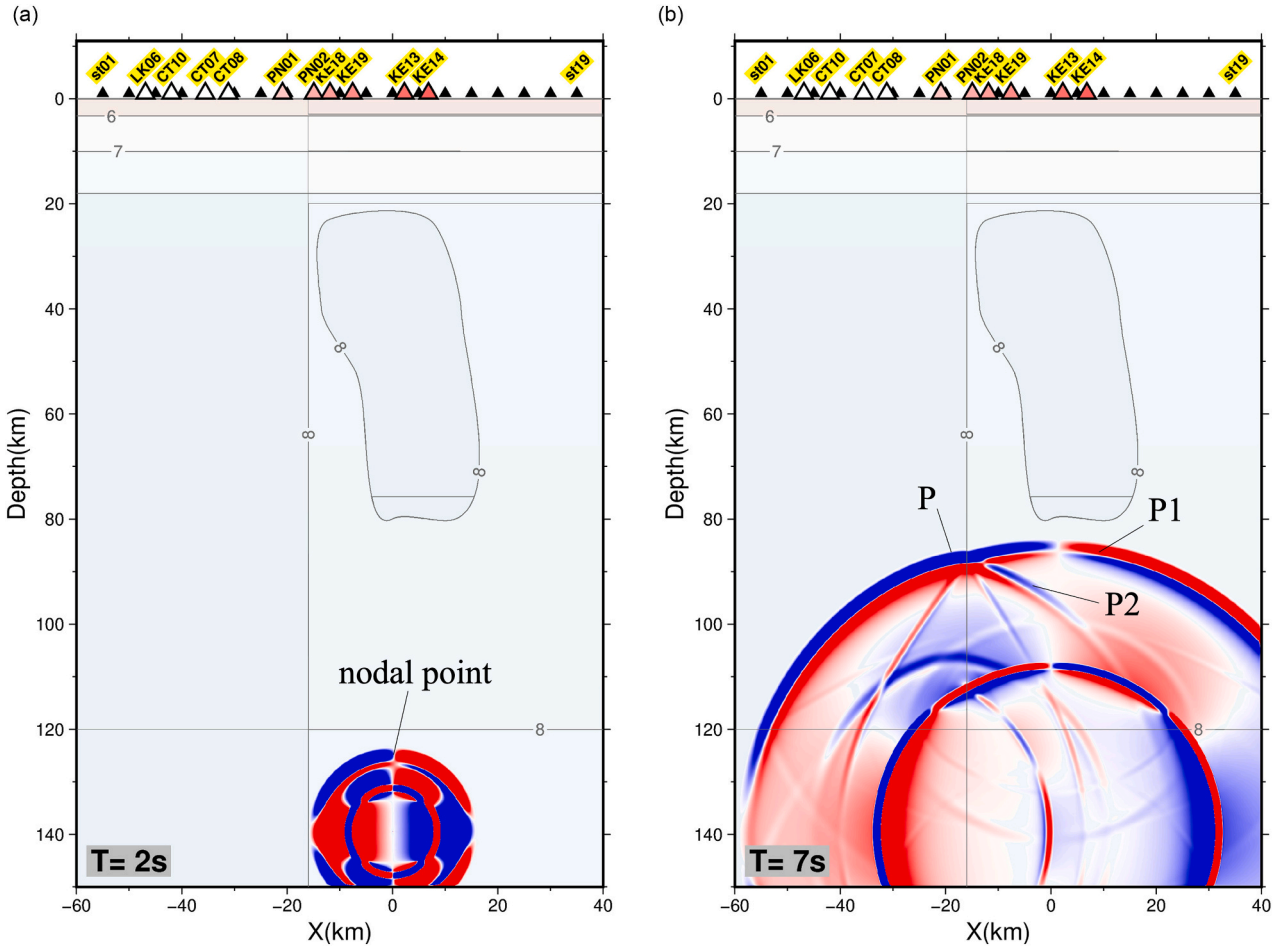

Fig. 6. Snapshots of 2D wave propagation from the source of 0312 event at 2, 7, 13, 16 s after the occurrence of the earthquake in panels (a), (b), (c), (d), respectively. Velocity contours, with numbers indicating velocity, are displayed. The locations of virtual stations and FA stations, colour-keyed according to delayed time, are shown at the top.

AA', which would indicate a crustal anomaly, are not observed in the dominant periods (around 1.5 s, as shown in Fig. 5). The waveforms are modeled without considering crustal anomalies, suggesting that their effect is minor. For (c), we assigned various Q values to the initial structure, specifically a high Q for regions with high V_P in the mantle wedge, and conducted a waveform simulation. The resulting waveforms exhibit only minor differences compared to those of a homogeneous Q model (Fig. S2).

As a final note, based on the mechanism proposed in this study, the onset of P2 or zero P1-P2 delay time represents the subvertical projection of the ELB, approximately 25 km west of the epicenter along AA'. The contour of zero P1-P2 delay time observed by all FA stations provides constraint into the boundary between the PSP and EUP at the surface (Fig. 1). It is noteworthy that the waveform-constrained ELB identified in this study is consistent with the NW termination of the PSP, as determined by the distribution of deep seismicity (orange line in Fig. 1, Ko et al., 2012), and lies to the east of the boundary proposed by Wu et al. (2009) (blue line in Fig. 1).

The surface projection of the ELB provides a means to distinguish between the active and passive roles of the EUP in accommodating the northwesterly-indented Philippine Sea Plate slab beneath northeast Taiwan. In the case of active detachment of the EUP slab, the ELB would pass northeast Taiwan in a nearly north–south trend (Teng, 1996). In contrast, for passive tearing of the EUP, the ELB would pass approximately along 24°N in an east–west trend (Lallemand et al., 2001). In addition to the boundary proposed by Ko et al. (2012) and Wu et al. (2009), the results of this study provide an alternative constraint that supports the active role of the EUP (Fig. 10a). Accordingly, we interpret the velocity structures along AA' as mainly resulting from previous EUP subduction, drawing an analogy with numerical modeling of crustal eclogitization in orogens (Fig. 3b of Krystopowicz and Currie (2013)). In Fig. 10b, H2 is expressed as the metamorphic eclogitization of the EUP crust. The results of Zhang et al. (2024) appear to be reasonably consistent with Vp anomalies of up to +8 % in eclogites relative to pre-eclogite hydrous subduction assemblages.

5. Conclusion

In this study, we reexamine data from the March 12, 2019, earthquake, as recorded by FA stations, to propose an alternative mechanism for the observation of two P phases. By compiling arrival time patterns and waveform characteristics, and selecting a representative 2D profile for simulation, we successfully reproduce the observations with satisfactory fitting. We conclude that the presence of a high Vp anomaly in the mantle wedge above the Ryukyu subduction zone, combined with a slightly faster Eurasian lithosphere to the west and a sub-vertical boundary (ELB), constitutes the structural sources of this mechanism. Consequently, the small amplitudes of P1 result from a near-nodal point in the earthquake's radiation pattern, while P2 corresponds to a head wave propagating along the sub-vertical ELB. The 2D model structures can also reproduce the arrival time patterns of other nearby events with observations of two P phases. The results of this study also provide

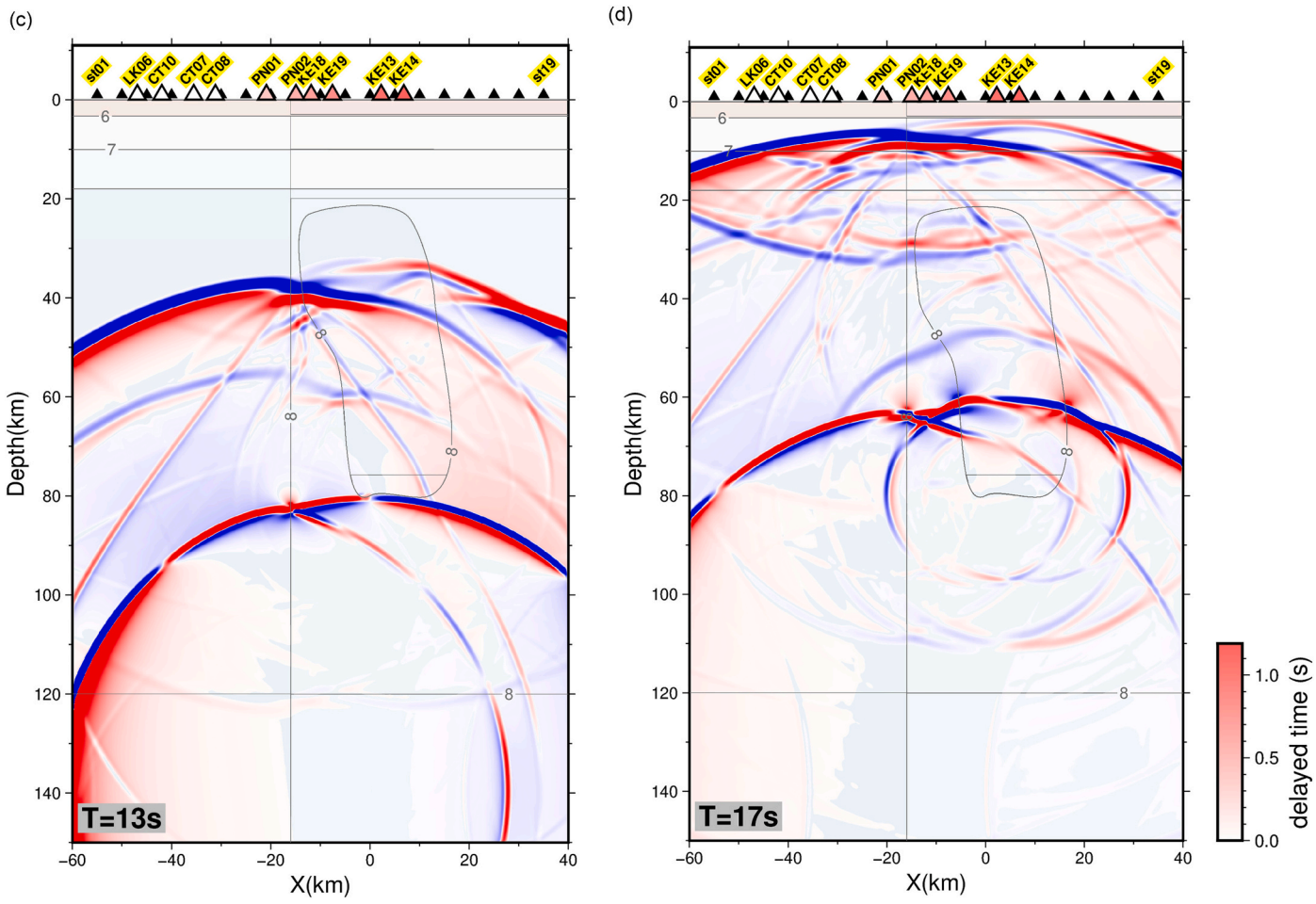

Fig. 6. (*continued*).

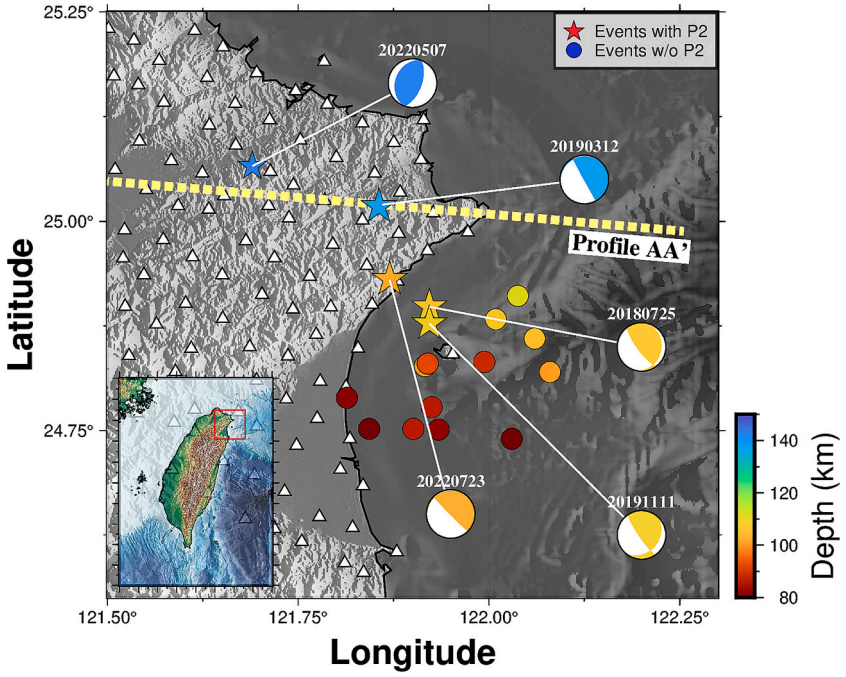

Fig. 7. Compilation of deep earthquakes (depth > 80 km) beneath Northeast Taiwan. Earthquakes with two first P-wave observations recorded by FA stations are indicated by stars, with AutoBATS focal mechanisms and dates shown (e.g., 20,190,312 for March 12, 2019). The red box in the inset highlights the search region. (For interpretation of the references to colour in this figure legend, the reader is referred to the web version of this article.)

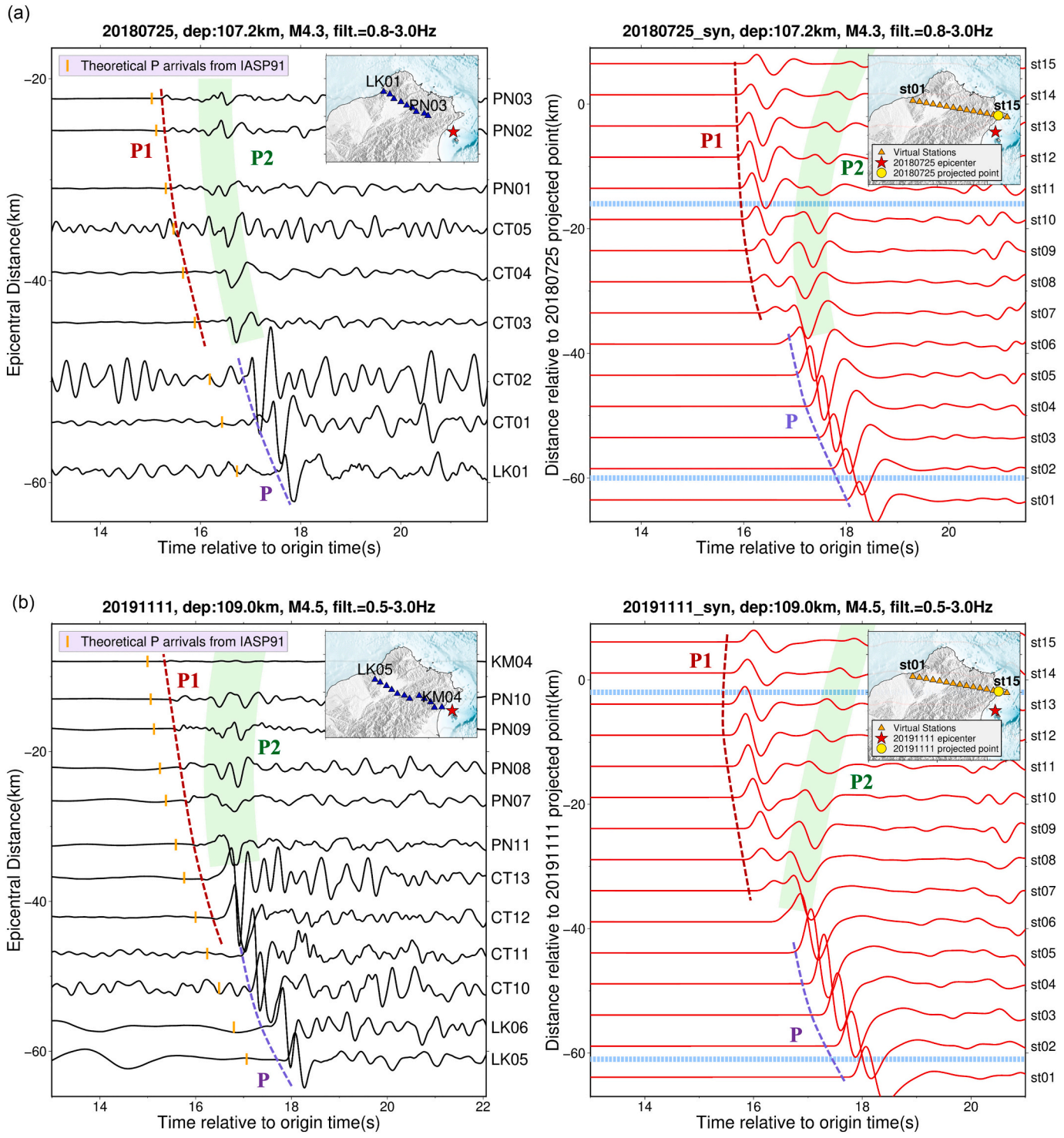

Fig. 8. Observations and simulations of events exhibiting two P phases are presented for (a) 20,180,725, (b) 20,191,111, (c) 20,220,723, and (d) 20,220,507. Please refer to Fig. 7 for the event locations. In each plot, the left panel represents observations from linear FA stations along the optimized azimuth shown at onset. The right panel displays synthetic data for virtual stations along the AA' profile. The corresponding range of observations is marked by dashed lines in light blue. The P, P1, and P2 phases are labeled for comparison. Note the source location of (d) and the two P phases occur to the west side of the array. (For interpretation of the references to colour in this figure legend, the reader is referred to the web version of this article.)

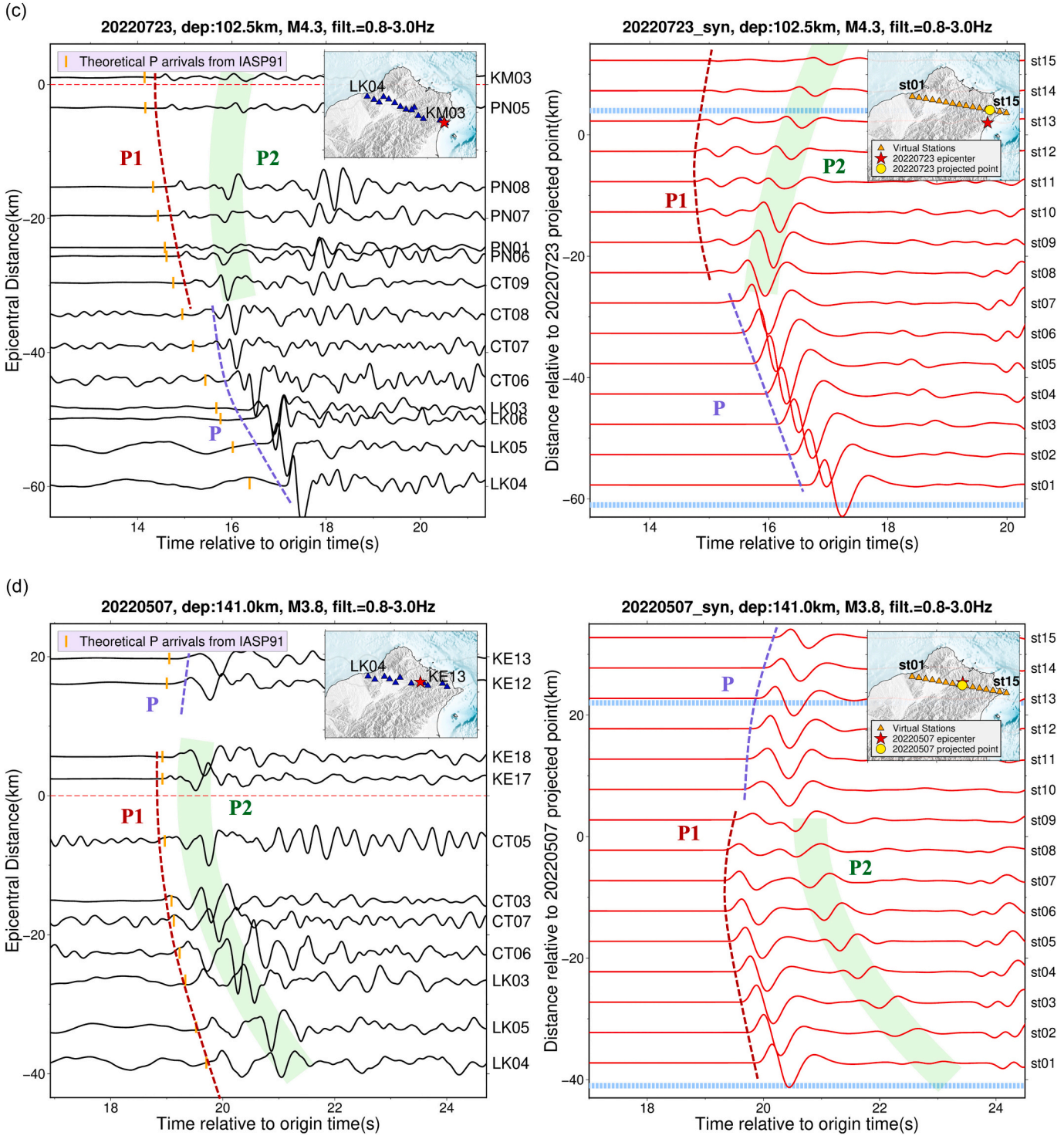

Fig. 8. (*continued*).

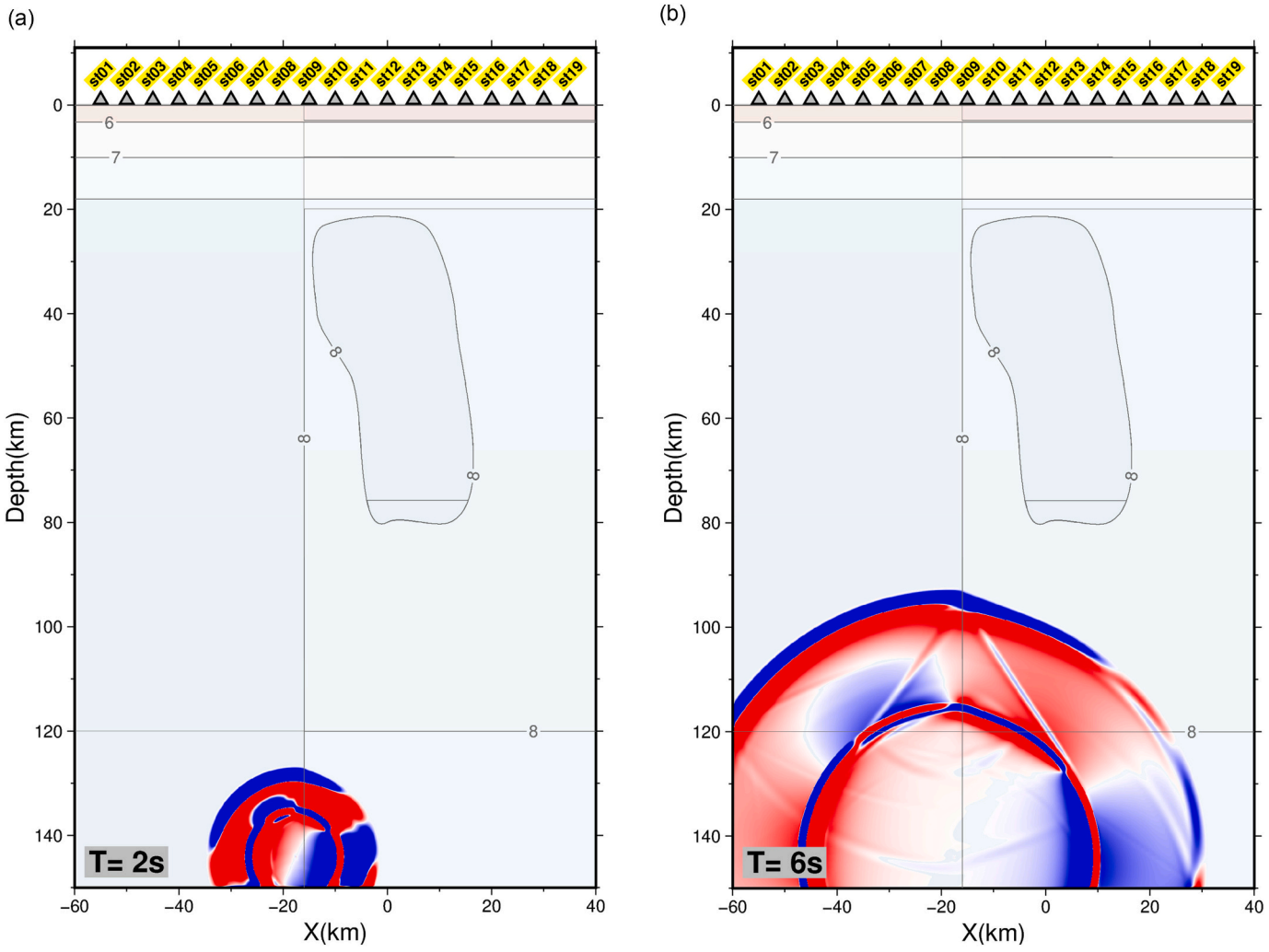

Fig. 9. Snapshots of 2D wave propagation from the source of 20,220,507 event at 2, 6, 12, 16 s after the earthquake in panels (a), (b), (c), (d), respectively. Velocity contours, with numbers indicating velocity, are displayed. Note that the epicenter is located to the west of ELB, resulting in the head wave along the west side of H2 with the P2 phase propagating upward to the west.

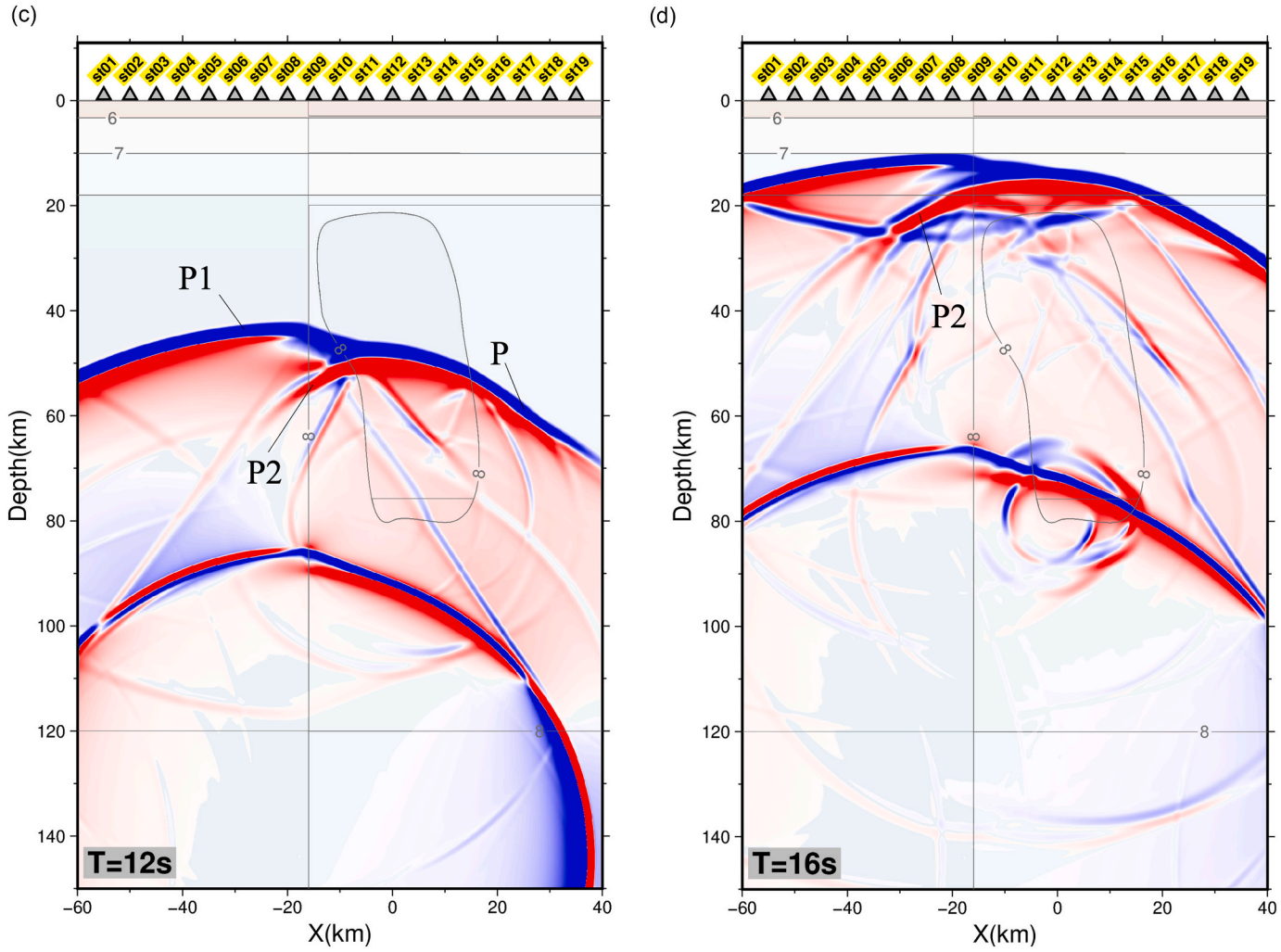

Fig. 9. (*continued*).

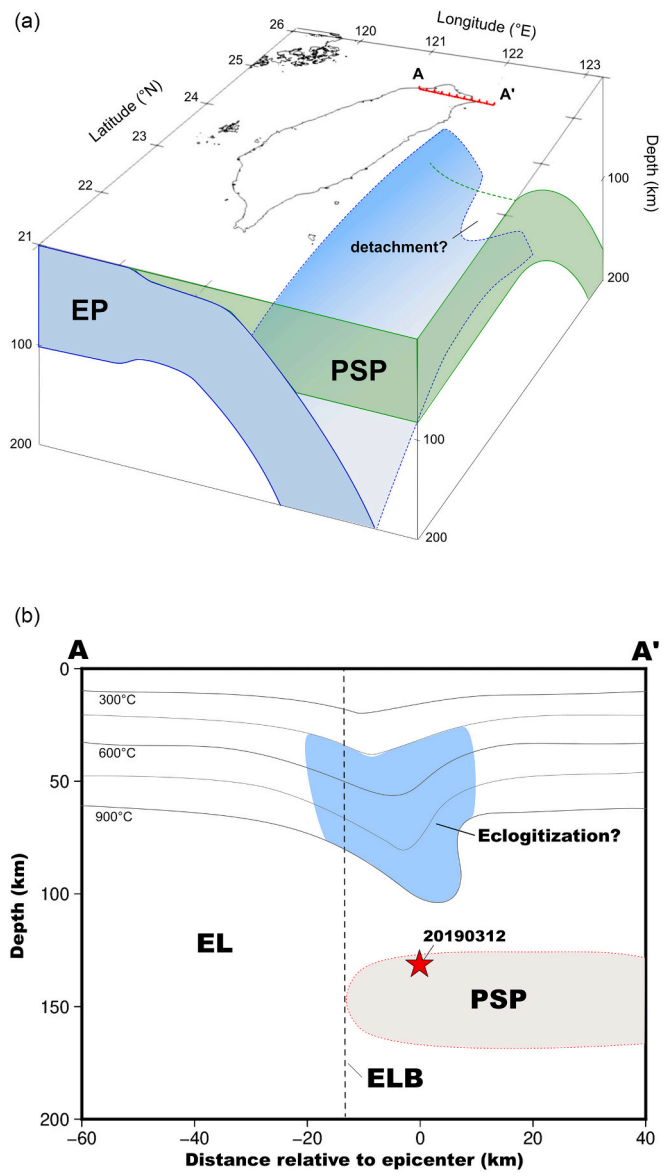

Fig. 10. Cartoon illustrating the geodynamics along AA'. (a) The configuration of the EUP and its interaction with the PSP are adapted from Fig. 4 of Huang et al. (2014) and Fig. 2b of Lin and Kuo (2016), respectively. Dashed blue lines represent the top of the EUP slab behind the PSP. (b) The temperature contours and the depiction of crustal eclogitization are referenced from Fig. 3b of Krystopowicz and Currie (2013). (For interpretation of the references to colour in this figure legend, the reader is referred to the web version of this article.)

alternative constraint on the boundary between the PSP and EUP at the surface.

Supplementary data to this article can be found online at https://doi.org/10.1016/j.pepi.2025.107409.

CRediT authorship contribution statement

Hung-Yu Yen: Visualization, Software, Methodology, Formal analysis, Data curation. **Po-Fei Chen:** Writing – review & editing, Writing – original draft, Supervision, Investigation, Funding acquisition, Conceptualization. **Mei Chien:** Software.

Declaration of competing interest

The authors declare the following financial interests/personal relationships which may be considered as potential competing interests.

Acknowledgements

We are grateful to Prof. Craig R. Bina for his input on Fig. 10. We thank Prof. D. Schutt and one anonymous reviewer for constructive comments. We acknowledge the FA (https://fmarray.earth.sinica.edu.tw/) for providing the data. This work was supported by the Taiwan Earthquake Research Center (TEC) funded through the National Science and Technology Council (NSTC) of Taiwan with Grant Number 113-2116-M-008-004. The TEC contribution number for this article is 00201. Some figures were prepared with the Generic Mapping Tools (Wessel and Smith, 1998).

Data availability

The authors do not have permission to share data.

References

Bina, C.R., Čížková, H., Chen, P.-F., 2020. Evolution of subduction dip angles and seismic stress patterns during arc-continent collision: modeling Mindoro Island. Earth Planet. Sci. Lett. 533, 116054. https://doi.org/10.1016/j. epsl.2019.116054.

Central Weather Administration (CWA, Taiwan), 2012. Central weather administration seismographic network [SEED data]. Int. Federation Digital Seismograph Networks. https://doi.org/10.7914/SN/T5.

Chen, P.-F., Huang, B.-S., Liang, W.-T., 2004. Evidence of a slab of subducted lithosphere beneath Central Taiwan from seismic waveforms and travel times. Earth Planet. Sci. Lett. 229, 61–71.

Ho, C.S., 1986. A synthesis of the geologic evolution of Taiwan. Tectonophysics 125 (1–3), 1–16. https://doi.org/10.1016/0040-1951(86) 90004-1.

Huang, H.-H., Wu, Y.-M., Song, X., Chang, C.-H., Kuo-Chen, H., Lee, S.-J., 2014. Investigating the lithospheric velocity structures beneath the Taiwan region by nonlinear joint inversion of local and teleseismic *P* wave data: slab continuity and deflection. Geophys. Res. Lett. 41 (18), 6350–6357. https://doi.org/10.1002/2014GL061115.

Institute of Earth Sciences, Academia Sinica, Taiwan, 2017. Formosa Array. Institute of Earth Sciences, Academia Sinica, Taiwan. Other/Seismic Network. https://doi.org/10.7914/SN/FM.

Jian, P.-R., Tseng, T.-L., Liang, W.-T., Huang, P.-H., 2018. A new automatic full waveform regional moment tensor inversion algorithm and its applications in the Taiwan area. Bull. Seismol. Soc. Am. 108 (2), 573–587. https://doi.org/10.1785/0120170231.

Kennett, B.L.N., Engdahl, E.R., Buland, R., 1995. Constraints on seismic velocities in the earth from traveltimes. Geophys. J. Int. 122 (1), 108–124. https://doi.org/10.1111/j.1365-246X.1995.tb03540.x.

Ko, Y.-T., Kuo, B.-Y., Wang, K.-L., Lin, S.-C., Hung, S.-H., 2012. The southwestern edge of the Ryukyu subduction zone: a high Q mantle wedge. Earth Planet. Sci. Lett. 335–336, 145–153. https://doi.org/10.1016/j.epsl.2012.04.041.

Krystopowicz, N.J., Currie, C.A., 2013. Crustal eclogitization and lithosphere delamination in orogens. Earth Planet. Sci. Lett. 361, 195–207. https://doi.org/10.1016/j. epsl.2012.09.056.

Lallemand, S., Font, Y., Bijwaard, H., Kao, H., 2001. New insight on 3-D plates interaction near Taiwan from tomography and tectonic implications. Tectonophysics 335 (3–4), 229–253. https://doi.org/10.1016/S0040-1951(01)00071-3.

Lin, C.-H., Shih, M., Lai, Y., 2019. A strong seismic reflector within the mantle wedge above the Ryukyu subduction of northern Taiwan. Seismol. Res. Lett. 91 (1), 310–316. https://doi.org/10.1785/0220190174.

Lin, C.-H., Shih, M.-H., Lai, Y.-C., 2021. Mantle wedge diapirs detected by a dense seismic array in northern Taiwan. Sci. Rep. 11 (1), 1561. https://doi.org/10.1038/s41598-021-81357-7.

Lin, S.-C., Kuo, B.-Y., 2016. Dynamics of the opposite-verging subduction zones in the Taiwan region: insights from numerical models. J. Geophys. Res. Solid Earth 121, 2174–2192. https://doi.org/10.1002/2015JB012784.

Maeda, Takuto, Takemura, S., Furumura, T., 2017. OpenSWPC: an open-source integrated parallel simulation code for modeling seismic wave propagation in 3D heterogeneous viscoelastic media. Earth Planets Space 69 (1), 102. https://doi.org/10.1186/s40623-017-0687-2.

Su, P., Chen, P., Wang, C., 2019. High-resolution 3-D *P* wave velocity structures under NE Taiwan and their tectonic implications. J. Geophys. Res. Solid Earth 124 (11), 11601–11614. https://doi.org/10.1029/2019JB018697.

Teng, L.S., 1996. Extensional collapse ofthe northern Taiwan mountain belt. Geology 24, 945–952.

Teng, L.S., Lee, C.T., Tsai, Y.B., Hsiao, L.-Y., 2000. Slab breakoff as a mechanism for flipping of subduction polarity in Taiwan. Geology 28 (2), 155. https://doi.org/10.1130/0091-7613(2000)28<155:SBAAMF>2.0.CO;2.

Wessel, P., Smith, W.H.F., 1998. New, improved version of the generic mapping tools released. EOS Trans. Am. Geophys. Union 79, 579.

Wu, F.T., Rau, R.J., Salzberg, D., 1997. Taiwan orogeny: thin-skinned or lithospheric collision? Tectonophysics 274, 191–220.

Wu, F.T., Liang, W.-T., Lee, J.-C., Benz, H., Villasenor, A., 2009. A model for the termination of the Ryukyu subduction zone against Taiwan: a junction of collision, subduction/separation, and subduction boundaries. J. Geophys. Res. 114 (B7), B07404. https://doi.org/10.1029/2008JB005950.

Wu, Y.-M., Chang, C.-H., Zhao, L., Teng, T.-L., Nakamura, M., 2008. A comprehensive relocation of earthquakes in Taiwan from 1991 to 2005. Bull. Seismol. Soc. Am. 98 (3), 1471–1481. https://doi.org/10.1785/0120070166.

Yu, S.-B., Chen, H.-Y., Kuo, L.-C., 1997. Velocity field of GPS stations in the Taiwan area. Tectonophysics 274, 41–59.

Zhang, R., Wang, D., Cai, N., Zhang, J., Chen, P., Han, K., Cao, Y., 2024. Sound velocity of eclogite at high pressures and implications for detecting eclogitization in subduction zones. GSA Bull. 136 (5/6), 2019–2028. https://doi.org/10.1130/B37065.1.

Zhang, W., Shen, Y., 2010. Unsplit complex frequency-shifted PML implementation using auxiliary differential equations for seismic wave modeling. Geophysics 75 (4), T141–T154. https://doi.org/10.1190/1.3463431.